Electron transport properties of mirror twin grain boundaries in molybdenum disulfide: Impact of disorder

Jejune Park, Kan-Hao Xue, Mireille Mouis, Francois Triozon, Alessandro Cresti

To cite this version:

Jejune Park, Kan-Hao Xue, Mireille Mouis, Francois Triozon, Alessandro Cresti. Electron transport properties of mirror twin grain boundaries in molybdenum disulfide: Impact of disorder. Physical Review B: Condensed Matter and Materials Physics (1998-2015), 2019, 100 (23), pp.235403. 10.1103/PhysRevB.100.235403 . hal-02390123

HAL Id: hal-02390123
https://hal.science/hal-02390123v1

Submitted on 19 Nov 2020

Electron transport properties of mirror twin grain boundaries in molybdenum disulfide: Impact of disorder

Jejune Park,[1, 2] Kan-Hao Xue,[1, 3] Mireille Mouis,[1] François Triozon,[2] and Alessandro Cresti[1]

[1] *Univ. Grenoble Alpes, Univ. Savoie Mont Blanc, CNRS,*
Grenoble INP, IMEP-LAHC, 38000 Grenoble, France
[2] *CEA, LETI, Minatec Campus and Université Grenoble Alpes, 38054 Grenoble, France*
[3] *School of Optical and Electronic Information, Huazhong University of Science and Technology, Wuhan 430074, China*

Grain boundaries in two-dimensional transition metal dichalcogenides can strongly affect the transport properties by reducing the electron mobility or allowing gap conduction through extended grain boundary states. Here, by combining advanced modeling tools — density-functional-theory-calibrated tight-binding Hamiltonians and Green's function techniques — we investigate transport along and across mirror twin grain boundaries in MoS_2. Our results show that the grain boundary conductive channels are strongly affected by sulfur vacancies, while short-range Anderson disorder has a moderate impact, which we quantitatively analyze, and long-range disorder has a very weak effect. As for transport across the grain boundaries, the system conductance turns out to be less than half that for the pristine system, and the spin-orbit coupling and intervalley scattering are found to play an important role. Our findings are beneficial to the understanding and the prediction of the impact of mirror twin grain boundaries in the transport phenomena, and could be of help in designing electronic devices based on transition metal dichalcogenides.

This is the self-archived version of the paper

J. Park, K.-H. Xue, M. Mouis, F. Triozon, and A. Cresti, Physical Review B **100**, 235403 (2019)

DOI: 10.1103/PhysRevB.100.235403

I. INTRODUCTION

After the discovery of graphene [1], a plethora of new two-dimensional (2D) materials with a great variety of electronic properties [2] have been predicted, fabricated and investigated. Among them, semiconducting 2D materials are in the limelight for their very promising electronic and optoelectronic applications [3, 4]. For example, field-effect transistors benefit from the few-atom thickness of 2D materials, which allows an enhanced electrostatic control, and from their self-passivated surfaces, where the absence of dangling bonds reduces the risk of traps at the interface with the oxide. Most importantly, the presence of a band gap in semiconducting 2D materials, in contrast with graphene [5], allows a much higher on/off current ratio in logic devices [4]. It also allows the design of tunnel field-effect transistors with lateral [3] and vertical [6] structures, as well as energy filtering steep-slope transistors [7]. The use of MoS_2 for topological quantum transistors was also proposed [8]. Furthermore, the van der Waals stacking of different materials [9] opens unprecedented possibilities for the realization of original and complex architectures. The most comprehensively investigated 2D materials beyond graphene are the semiconducting transition metal dichalcogenides (TMDs) [10]. In particular, monolayers from group VI in the trigonal prismatic phase show sizable direct band gaps. Some years after the first realization of a working MoS_2-based transistor [11], transistors based on TMD van der Waals heterostructures [9, 12] were demonstrated, which represent a significant advance towards completely 2D microprocessors [13].

For applications, a large-scale fabrication of large-area TMDs is crucial. In this respect, chemical vapor deposition (CVD) [14–16] has emerged as a very efficient growth technique, which is promising for industrial production. However, CVD TMDs may present several kinds of defects, which are expected to significantly impact the electronic and transport properties, with possible degradation of the device performance. The most common defect is the polycrystallinity of CVD TMDs, which is inherent in the synthesis process. The grain boundaries at the interfaces between crystalline grains have been reported to strongly localize electrons [17], with consequent carrier mobility degradation [18, 19]. Therefore, understanding the impact of grain boundaries on the transport properties of TMDs is of central importance.

Among the huge variety of grains boundaries with different geometries, mirror twin grain boundaries (MTBs) are commonly observed in experiments [16, 20, 21]. An MTB is an inversion grain boundary that forms at the interface between two grains with a 60° rotation angle. Interestingly, density functional theory (DFT) calculations [16, 21, 22] reveal that a periodic MTB shows dispersive and metallic states within the bulk gap of the two-dimensional semiconducting TMDs, while most of the tilt grain boundaries induce strongly localized states [19]. Such a metallic nature has also been experimentally demonstrated by scanning tunneling spectroscopy [23]. With regard to field-effect transistor applications, metallic MTBs along the transistor channel may result in a detrimental leakage current flowing through the TMD gap. On the other hand, metallic MTB networks could drive opportunities for the realization of suited metallic contacts for semiconducting TMDs, as experimentally demonstrated [24]. In the literature, however, electron transport in the presence of MTBs has been barely investigated theoretically, with existing studies mainly focusing on transport across periodic and defect-free grain boundaries [21, 25, 26].

In this paper, by means of calculations of the Landauer-Büttiker conductance [27] based on the Green's function approach and a DFT-calibrated tight-binding (TB) model, we explore electron quantum transport along and across a metallic MTB in MoS_2. In particular, we investigate the robustness of the MTB conductive channels against short-range and long-range disorders. Then, we concentrate on the conductance of 2D MoS_2 where the MTB is orthogonal to the transport direction, and provide a physical understanding of the transport degradation. Our main result is a full analysis of the impact of MTBs on the transport properties of MoS_2. Note that low-temperature many-body effects, such as charge density wave transition [28, 29] and Tomonaga-Luttinger liquid phase [30], are out of the scope of our study.

The paper is organized as follows. Section II introduces the model and details the electronic structure of the MTB. In Sects. III and IV, we investigate electron transport along and across an MTB, respectively. Section V concludes. Finally, the details of DFT simulations and TB model, as well as of the scaling analysis of the transport properties in the presence of disorder are reported in the Appendices.

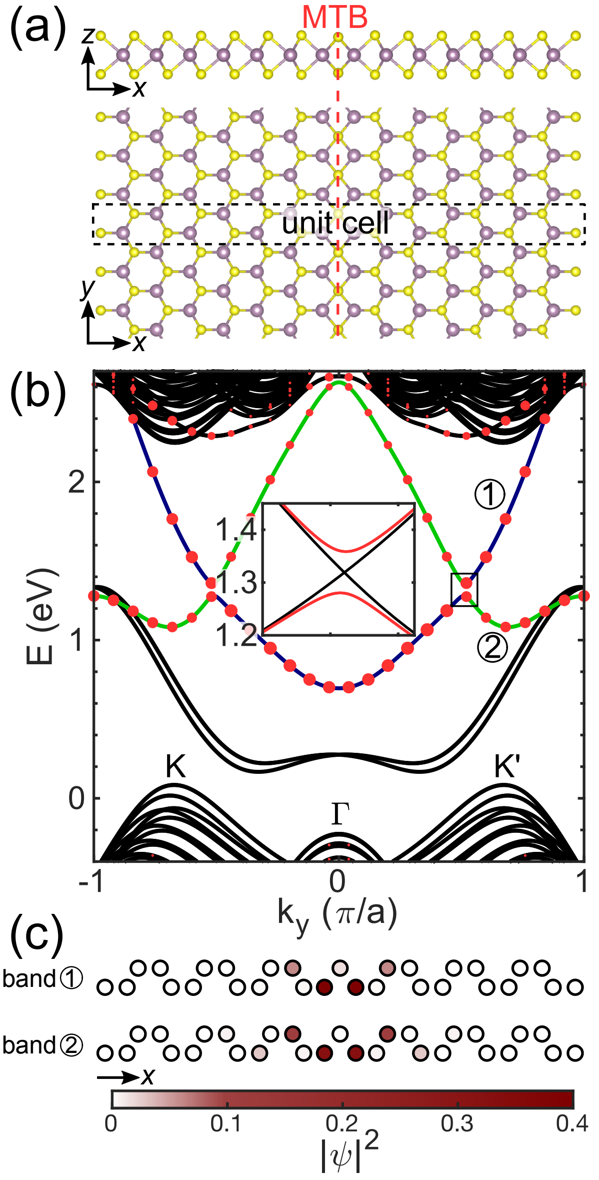

FIG. 1. (a) Side and top views of the relaxed atomic structure of a periodic MTB, highlighted by a dashed red line, in MoS_2. Mo atoms are in purple color and S atoms are in yellow color. The dashed rectangle indicates a unit cell for the ribbon, which is periodic along the y-direction and whose lattice parameter is $a = 0.316$ nm. (b) Band structure obtained with the calibrated TB model of a zigzag ribbon with width $W = 10$ nm and a periodic MTB along its axis. ① and ② indicate the two spin-degenerate MTB bands within the bulk gap, which are highlighted by blue and green lines. The size of the red dots corresponds to the weight of the states on the molybdenum atoms in the MTB region. The indicated K, K' and Γ points correspond to the projection of the corners and the center of the hexagonal Brillouin zone of 2D MoS_2 onto the 1D Brillouin zone of the ribbon. Inset: Band structures with (red line) and without (black line) SOC in the region indicated by a square. The energy gap induced by SOC is ~80 meV, which is close to that found by DFT calculations, see fig. 9 for more details. (c) Probability density of the states at $E = 2$ eV on bands ① and ② on the atoms close to MTB.

II. ELECTRONIC STRUCTURE OF THE MIRROR TWIN BOUNDARY

We consider MoS_2 ribbons with a periodic MTB along their axis in the y-direction. We focus on the rather common geometry called 4|4 P [16], whose relaxed structure calculated by DFT is shown in fig. 1(a). DFT calculations were carried out using the plane-wave basis set and the projector augmented-wave method, and the generalized gradient approximation of the Perdew-Burke-Ernzerhof functional form [31], as implemented in the Vienna *Ab initio* Simulation Package [32, 33], see Appendix A for more details. Note that the MTB is along the zigzag direction, which implies that edges are along the zigzag orientation.

To describe the MTB, we make use of a TB Hamiltonian, which can take into account the atomistic details of the structure modulation induced around the grain boundary. We adopt the Slater-Koster [34] TB parametrization of Ref. [35], which considers five d orbitals for Mo atoms and three p orbitals for S atoms. This TB model has the advantage of not being based on symmetry considerations [36] and therefore to be able to reasonably describe geometrically distorted configurations. Moreover, it is accurate for energies within approximately 1 eV from the valence and conduction band edges.

We introduce the effect of spin-orbit coupling (SOC), which is known to play an important role in TMDs, by appropriate intra-atomic Hamiltonian elements [37]

$$H_{\mathrm{SOC}} = \sum_{\alpha} \frac{\lambda_\alpha}{\hbar} \hat{L}_\alpha \cdot \hat{S}_\alpha \ , \tag{1}$$

where α is the atom index, $\hat{L}$ is the atomic orbital angular momentum operator, $\hat{S}$ is the spin operator, and λ_α is the intra-atomic SOC constant with value 75 meV for Mo atoms and 52 meV for S atoms [37]. The use of the Slater-Koster TB model allows us to consider the effect of strain, which is present in our case due to the lattice deformations close to the MTB. The two-center energy integral elements V_{ij} between two orbitals i and j depend on the interatomic distance d as [39]

$$V_{ij}(d) = V_{ij}(d_0) \left(\frac{d_0}{d} \right)^{\gamma_{ij}} \ , \tag{2}$$

where d_0 is the unstrained interatomic distance for the given couple of atoms corresponding to the i and j orbitals, and γ_{ij} is a parameter, which can be assumed as $\gamma_{ij} = l_i + l_j + 1$ with l_i and l_j the angular momenta of the orbitals i and j, respectively [38]. Together with the relaxed geometry obtained from DFT calculations, this provides an accurate description of the effect of strain induced by the MTB.

The resulting Hamiltonian fairly reproduces the DFT shape of the bands corresponding to the MTB, but not their energy position. This problem is solved by a further calibration procedure, which consists in analyzing the specific orbital contributions to each band and in modifying the on-site energies of some properly selected orbitals. The result of the calibration, which is detailed in Appendix B, is a shift by +1 eV, +0.2 eV, -0.3 eV and -0.8 eV of the on-site energies of the d_{zx}, d_{yz}, d_{xy} and d_{z^2} orbitals of the Mo atoms nearest to the MTB.

Figure 1(b) shows the band structure of a zigzag ribbon with width $W = 10$ nm and a periodic MTB along its axis. These results are comparable with those previously obtained in the literature by DFT calculations [30]. The electronic structure consists of bulk bands, with direct gap at the K and K' points, which appear as quantized subbands due to lateral confinement, and dispersive bands within the bulk gap. Among these latter, in addition to those corresponding to edge states, we find those (indicated by red dots) corresponding to MTB states. The two MTB spin-degenerate bands within the bulk band gap, indicated by ① and ② in fig. 1(b), display different properties in terms of wave functions and atomic orbital compositions. In particular, band ① exhibits a narrow wave function (with width up to ∼0.8 nm) composed of d_{yz} and d_{zx} Mo orbitals, while band ② shows a spatially more extended wave function (with width up to ∼1.3 nm) mainly stemming from d_{xy}, d_{z^2} and d_{x^2} orbitals of Mo atoms, see fig. 1(c) and Appendix B.

We would like to comment on the effect of SOC, which is responsible for the anticrossing of the two MTB bands and the opening of a small gap in the order of 80 meV, see the inset of fig. 1(b). This feature is also observed in the DFT calculations, see fig. 9(b) in Appendix B, where the results with and without SOC clearly show the band anticrossing and crossing, respectively. The anticrossing is the consequence of the hybridization between two MTB bands induced by the SOC coupling of the different orbitals composing the two bands. Note that the bands are spin-degenerate, because, in contrast with the pristine MoS_2, in the presence of the MTB the system is invariant under inversion symmetry. Together with the time-reversal symmetry, this entails the Kramers degeneracy of the bands. While for the whole ribbon the presence of the inversion symmetry requires the MTB to be exactly along the ribbon axis (as in our case), such a symmetry always holds for the region around the grain boundary itself. As a consequence, the spin-degeneracy of the MTB dispersive states within the bulk band gap is expected to be generally observed.

Let us now analyze how bulk states outside the bulk band gap are affected by the MTB. As shown in fig. 2(a), the shape and the spacing of the quantized bulk valence bands for the ribbon in the presence of the MTB are comparable to those of a pristine ribbon with a half-width, i.e., $W = 5$ nm. This indicates that the MTB has the effect of “cutting” the ribbon into two narrower ones. The weak coupling between these resulting two ribbons induces a small modification of the valence bands, as observed in the figure. Note that while the bands of the ribbon with the MTB are spin-degenerate, the pristine ribbon bands are spin-split due to the joint effect of SOC and absence of inversion symmetry. A more detailed physical understanding can be gained by looking at the local density of states (LDoS) displayed in fig. 2(b) as a function of the energy and of the x-position across the ribbon. The MTB is located in the center at $x = 0$ nm. In agreement with the band structure of fig. 1(b), the LDoS exhibits MTB states within the bulk band gap, while it vanishes away from $x = 0$ nm. More importantly, as shown as the dashed circle in fig. 2(b), the LDoS turns out to be relatively low in the vicinity of the MTB in the valence band, thus illustrating and confirming the effective separation of the ribbon into two narrower ribbons. This effect also significantly affects the transport properties, as we will discuss in Sec. IV.

III. TRANSPORT ALONG THE MIRROR TWIN BOUNDARY

In this section, we investigate electron transport along the MTB, i.e., along the y-axis, in the energy region of the bulk gap, where the grain boundary states are active and surrounded by an insulating bulk. To calculate the Landauer-Büttiker conductance [27] we make use of home-grown numerical codes based on the Green’s func-

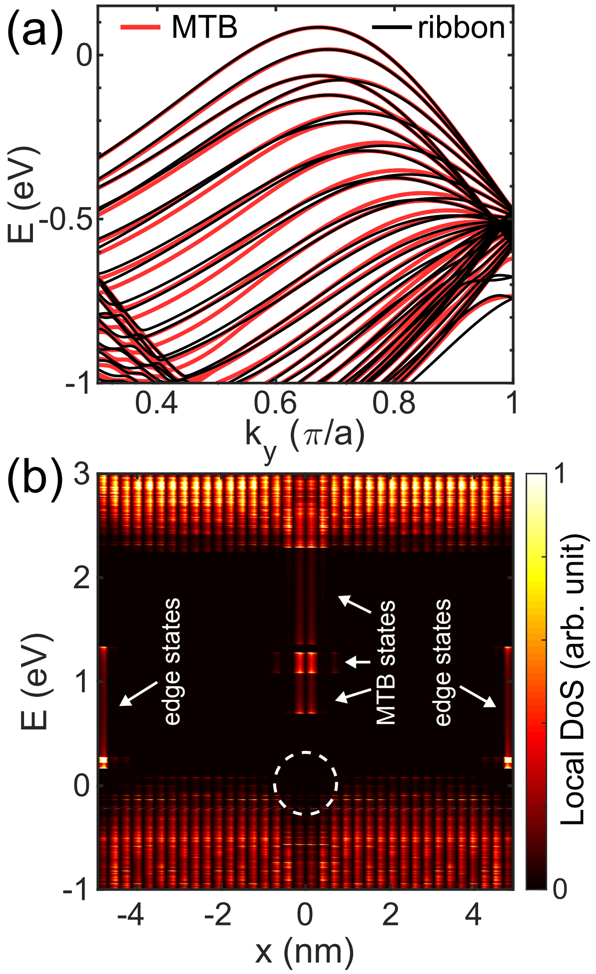

FIG. 2. (a) Band structures of a zigzag ribbon with $W = 10$ nm and the MTB along its axis (same as in fig. 1) and for a pristine zigzag ribbon with half-width $W = 5$ nm. Only the valence band region is shown. (b) Local density of states of the ribbon with an MTB as a function of the x-coordinate along the ribbon transverse section and the electron energy E. Edge states and MTB states within the bulk gap are indicated in white arrows. A white dashed circle displays the region with reduced density of states on the MTB.

tion approach, which allows us to write the transmission coefficient as [40]

$$T(E) = \mathrm{Tr}\left[\ \Gamma_\mathrm{S}(E)\ G^\mathrm{R}(E)\ \Gamma_\mathrm{D}(E)\ G^\mathrm{A}(E)\ \right]\ , \tag{3}$$

where Tr is the trace operator, E is the electron energy, G^R and G^A are the retarded and advanced Green's function matrices, Γ_S and Γ_D are the rate operator matrices for the source and drain contacts obtained from semi-infinite periodic prolongation of the system along the y-axis. The Green's function also provides the LDoS, i.e., the density of states on each atom as

$$\rho_n(E) = -\frac{1}{\pi}\mathrm{Im}\left\{\mathrm{Tr}\left[G_n^\mathrm{R}(E)\right]\right\}\ , \tag{4}$$

where G_n^R is the matrix of the retarded Green's function projected on the subspace of the orbitals of the atom with index n. Additional details about the numerical methods are given elsewhere [41, 42].

More specifically, this section focuses on the study of the robustness of the MTB conductive channels against additional short-range disorder (single sulfur vacancies and Anderson disorder) and long-range (Gaussian) impurities. We will provide a quantitative scaling analysis in terms of the different (quasi-ballistic, diffusive and localized regimes) transport regimes. Before proceeding, we would like to recall that, for an infinite periodic ribbon with an MTB but no additional disorder, the transmission coefficient is quantized at values corresponding to the number of active conductive channels at given energy. To focus on the MTB transmission and suppress the contribution of the ribbon edge states, which would complicate the analysis, we introduced edge roughness with amplitude 0.25 nm over a length of at least 20 nm. For wide enough ribbons and for energies within the bulk gap, as in our case, such an edge roughness does not affect the transport along the MTB at all but completely localizes the edge states with a localization length in the order of few nanometers [43]. As a result, the complete suppression of the edge transmission allows us to exclusively focus on the transmission of the MTB, see the dashed line of fig. 3(b).

A. Sulfur vacancies

Sulfur vacancies, as one of the most common defects observed in experiments, are expected to induce localized midgap states, which can significantly affect transport [44]. These vacancies could be fatal for the conductive MTB channels within the bulk gap.

To investigate this aspect, we introduce one single sulfur vacancy at different distances from the grain boundary, see fig. 3(a). The impact of the single sulfur vacancy is expected to be negligible when the vacancy is far enough from the grain boundary, because the localized vacancy states and the MTB states are spatially separated. Indeed, we do not find any impact of the vacancy when its distance d from the MTB is larger than ~ 1.4 nm. This is consistent with the fact that the vacancy states have a spatial extension of about 0.5 nm [44], while the MTB states have a maximum extension of about 1.3 nm. For shorter distances and down to $d \approx 0.6$ nm, the MTB transmission shows some dips around specific energies, see fig. 3(b). Such dips are a clear indication of resonant scattering between the MTB states and the localized vacancy states, as confirmed by the correspondence between the dip energies and the energy of the vacancy states, see the dashed lines in fig. 3(c). When the vacancy is closer to the grain boundary ($d = 0.3$ nm), its impact is much more effective and the transmission decreases over the whole energy range. Interestingly, when the sulfur vacancy is exactly placed

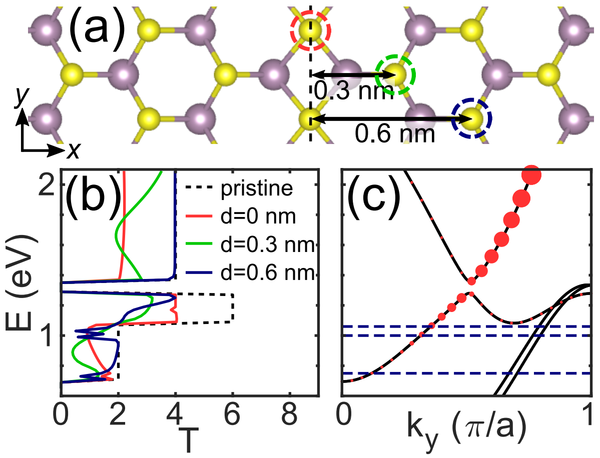

FIG. 3. (a) Three sulfur vacancy positions, indicated by circles, at different distances d from the MTB. (b) Transmission coefficient as a function of energy for the pristine system and in the presence of a single sulfur vacancy at the three positions specified in (a). (c) Band structure of the pristine ribbon in the bulk gap region. The size of the dots indicates the weight of the sulfur component of the corresponding states, which is only present for band ①. The dashed lines indicate the energies of the localized sulfur vacancy states.

on the grain boundary, we observe a strong suppression of two conductive channels for energies $E > 1.1$ eV, as demonstrated by the nearly quantized transmission coefficient $T \approx 4$ and $T \approx 2$ compared to $T = 6$ and $T = 4$ for the pristine system. We find that the suppressed conductive channels correspond to the MTB spin-degenerate band ①, which is contributed by the sulfur atoms. The sulfur weight in the wave functions is indicated by dots in fig. 3(c). Note that contribution of sulfur orbitals to the MTB states is much smaller than that of molybdenum orbitals, and that the size of dots in figs. 1(b) and 3(c) does not correspond to the same weight scale. Sulfur orbitals hardly contribute to band ②, which is active for $E \gtrsim 1.1$ eV, and thus the corresponding conductive channel is not appreciably affected by the vacancy.

For the sake of completeness, we estimated the formation energy for the single sulfur vacancies at the three considered positions displayed in fig. 3(a). More details about the DFT calculations are reported in Appendix A. The most probable vacancy position is far from the MTB ($d = 0.6$ nm), with a formation energy of 1.56 eV. The vacancies with $d = 0.3$ nm and $d = 0$ are energetically less favorable, with a formation energy of 2.39 eV and 1.95 eV, respectively.

B. Anderson disorder

The short-range Anderson disorder [45] introduces a random potential energy for each atom with value in the range $[-\Delta, \Delta]$, where Δ is the disorder strength. Despite its simplicity, such a popular disorder model allows a general physical understanding. Figure 4(a) shows an example of generated random on-site potentials with strength $\Delta = 100$ meV applied over a ribbon section of length L. To better statistically analyze the different transport regimes, we consider an ensemble of 100 Anderson disorder realizations for each case under study. Figure 4(b) reports the transmission coefficient for the pristine MTB and the average transmission coefficients $\langle T \rangle$ in the presence of Anderson disorder as a function of the electron energy E within the bulk band gap for $\Delta = 100$ meV and different lengths L. We can identify three energy regions, indicated in fig. 4(b) by the letters A (for $E \lesssim 1.1$ eV), B (for 1.1 eV $\lesssim E \lesssim 1.29$ eV, i.e., below the SOC-induced gap) and C (for $E \gtrsim 1.37$ eV, i.e., above the SOC-induced gap). In region A, only band ① is active and the decrease of $\langle T \rangle$ with L is exponential for $L > 100$ nm. This suggests a transition to the localized transport regime, for which the average logarithm of the transmission coefficients, $\langle \ln T \rangle$, scales as

$$\langle \ln T \rangle \propto -L/\xi \;, \tag{5}$$

where ξ is the localization length, and which is characterized by a Gaussian frequency distribution of $\ln T$, with $|\Delta \ln T / \langle \ln T \rangle| < 1$, where $\Delta \ln T$ is the standard deviation [46]. We verified that these conditions are satisfied, see Appendix C, and found that $\xi \approx 25 - 80$ nm. Such a localization length entails a huge transmission suppression when L is hundreds of nm. In region B, where six conductive channels are active, i.e., when both bands ① and ② contribute and the energy is below the SOC-induced gap, $\langle T \rangle$ decreases more slowly with increasing L, as shown in fig. 4(b). This suggests that the system is in the diffusive transport regime, which is characterized by a mean free path ℓ such that

$$\langle T \rangle \;=\; \frac{N}{1 + L/\ell} \;, \tag{6}$$

where $N = 6$ is the number of active conductive channels, and by a Gaussian frequency distribution of T, with $\Delta T / \langle T \rangle < 1$, where ΔT is the standard deviation [46]. These conditions are verified, see Appendix C, and the mean free path ℓ is found to range between 20 nm and 50 nm. Finally, the average transmission coefficient decreases very slowly in region C, which indicates that the system is in transition from the quasi-ballistic to the diffusive transport regime, as evidenced by the extremely large estimated mean free path up to ∼0.8 μm. Therefore, the MTB conductive channels for these energies are expected to be robust against Anderson disorder, and to stay in the quasi-ballistic transport for L in the order of hundreds of nm ($L < \ell$) and in the diffusive regime for L in the order of a few μm.

The mean free path ℓ as a function of the energy E is reported in fig. 4(c) for different disorder strengths Δ. The energies for which ℓ is not defined correspond to the SOC-induced gap or to regions where the transport

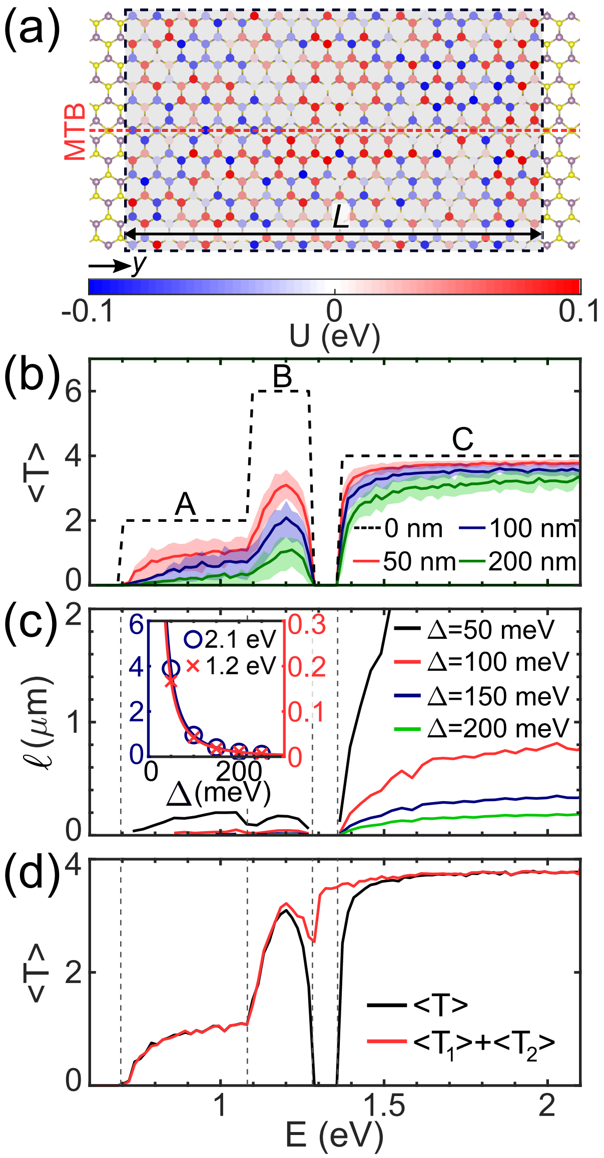

FIG. 4. (a) Example of Anderson disorder realization with random on-site energies for the atoms over the section of length L, and with strength $\Delta = 100$ meV. The MTB is highlighted by a dashed red line. (b) Average transmission coefficient as a function of the electron energy E for the MTB system in the pristine case ($L = 0$ nm) and in the presence of Anderson disorder with $\Delta = 100$ meV and L varying from 50 nm to 200 nm. The continuous lines and shaded regions show the average and the 25th to the 75th percentile of the transmission over 100 disorder realizations, respectively. (c) Mean free path as a function of E for different Anderson disorder strengths Δ. Inset: Mean free path as a function of Δ for two representative energies $E = 1.2$ eV and $E = 2.1$ eV. The continuous lines correspond to the fit $\propto \Delta^{-2}$. (d) Average transmission coefficient as a function of E for the MTB system in the presence of Anderson disorder with $\Delta = 100$ meV and $L = 50$ nm, and sum of the average transmission of the two MTB bands. $\langle T_1 \rangle$ is the average transmission of band ① contribution and $\langle T_2 \rangle$ is that of band ②.

regime is localized. The mean free path scaling with the Anderson disorder strength Δ is reported in the inset of fig. 4(c) for two representative energies $E = 1.2$ eV and $E = 2.1$ eV (in regions B and C, respectively), where the transport regime is diffusive. We find that ℓ is inversely proportional to Δ^2 for both representative energies. Such a behavior is consistent with a weak scattering regime, where the Fermi golden rule is a good approximation and yields a scattering probability proportional to Δ^2.

The origin of the different behaviors observed in the three regions can be understood by noting that bands ① and ② contribute independently to the transport properties. Indeed, by properly modifying the Hamiltonian, see Appendix D, it is possible to selectively shift band ① or band ② to higher energies and analyze the transport properties of each of the two bands individually. Figure 4(d) demonstrates that the total average transmission is given by the sum of the average transmission of the two bands, i.e., $\langle T \rangle \approx \langle T_1 \rangle + \langle T_2 \rangle$, except, of course, around the SOC gap, where the two bands hybridize. This means that Anderson disorder does not introduce any significant scattering between these two bands with different orbital compositions, and that we can analyze each band independently. In the first energy region ($E \lesssim 1.1$ eV), the short mean free path and the transition to the localization transport regime are due to the fact that electrons are at the bottom of band ①. Therefore, Anderson disorder is more effective in inducing intraband scattering. At higher energies, in the region B and even more above the SOC gap, the wave number separation between counter-propagating states in band ① becomes larger, thus significantly tempering the backscattering. In the region B, band ② provides four conductive channels. However, again, the small separation in the Brillouin zone (BZ) between counter-propagating states significantly enhances backscattering, especially close to the bands extrema, i.e., at the van Hove singularities. As a consequence, in this energy region the main contribution to transport comes from band ①. Analogously to what is observed for band ①, in region C above the SOC gap, the backscattering for the two conductive channels from band ② is strongly and progressively suppressed at higher energies. The resulting transmission coefficient is close to the ballistic case.

C. Long-range disorder

We now consider the impact of long-range disorder, which corresponds to real-space potential energy fluctuations induced, for example, by the presence of charged impurities in the substrate underlying the 2D material. Adam *et al.* [47] proposed a model of the potential profile $U(\mathbf{r})$ for graphene as a random distribution of Gaussian long-range scatterers

$$U(\mathbf{r}) = \sum_{i=1}^{N} \epsilon_i e^{\frac{-(\mathbf{r}-\mathbf{R}_i)^2}{2\chi^2}} , \tag{7}$$

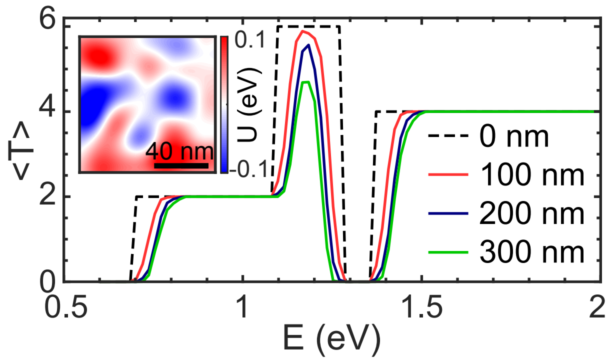

FIG. 5. Main panel: Average transmission coefficient as a function of the energy and for different L in the case of a SiO_2 substrate. The averaging is performed over 100 disorder realizations. Inset: Example of long-range potential profile realization for a SiO_2 substrate.

where i is the impurity index, $\mathbf{R}_i$ is its random position, ϵ_i is a randomly chosen potential energy that we select in the range [-Δ,Δ], N is the total number of Gaussian impurities and χ denotes the spatial range. Here, we consider two energy potential profiles corresponding to SiO_2 and hBN substrates. We adopt the parameters available in the literature for graphene [48], which are $\Delta = 50$ meV, $\chi = 10$ nm and $n = 10^{12}$ cm^{-2} for SiO_2, and $\Delta = 5$ meV, $\chi = 30$ nm and $n = 10^{11}$ cm^{-2} for hBN, where n is the density of impurities *per* surface area. These parameters may be different for MoS_2, but this effective model nonetheless provides a physical understanding of the impact of long-range disorder on the transport properties of MTBs.

The inset of fig. 5 shows the potential profile reproducing the effect of the SiO_2 substrate. We consider such a potential to be active over a section of the system with length L. The transmission coefficient averaged over 100 different profile realizations for different L is reported in the main panel of fig. 5. We observe a huge suppression of the transmission only close to edges of the transmission plateaus, where conductive channels are activated or deactivated. This behavior is explained by the fact that the long-range disorder over the quasi-1D MTB states induces local shifts of grain boundary bands along the system. In particular, the band edges, which determine the activation of the conductive channels, are smoothly shifted all along the grain boundary. The regions with the highest and lowest shifts, which tend to be about ±Δ for long enough L, determine the energy width of the decreased transmission region, as observed in the main panel of fig. 5. For the hBN substrate, not shown here, we do not observe any significant impact on the transport properties because of the extremely weak disorder strength Δ.

IV. TRANSPORT ACROSS THE MIRROR TWIN BOUNDARY

We now investigate the degradation of the electronic transmission of a two-dimensional MoS_2 layer in the presence of an MTB across the transport x-direction. Note that the two-dimensional system is infinitely extended in the x-direction, where the semi-infinite pristine regions at the sides of the MTB act as contacts, and periodic along the y-direction, which allows us to introduce the wave number k_y. We can thus calculate the transmission coefficient $T(E, k_y)$ for given energy E and wave number k_y, and obtain the zero-temperature conductance *per* unit of width by integration over the one-dimensional BZ as

$$g(E) = \frac{e^2}{h} \frac{1}{2\pi} \int_{\mathrm{BZ}} T(E, k_y)\, dk_y \ . \tag{8}$$

Figure 6(a) compares the conductance *per* unit of width for pristine MoS_2 and in the presence of the MTB. Of course, there is no transmission in the energy region of the gap, since no state is available for injecting electrons. We observe a general degradation of the conductance with a more than 50% reduction.

Interestingly, as already observed in the literature [26], the conductance is completely suppressed over about 150 meV from the top of the valence band, which corresponds to the SOC-induced splitting of the valence band in 2D MoS_2 [35], see the inset of fig. 6(a). In this energy region, the bands have opposite spin polarization at opposite K/K' valleys in each of the two grains on the two sides of the MTB. Note that the spin polarization is opposite in the two grains because of the mirror reflection symmetry of the system. Therefore, as a consequence of spin conservation, the current can only flow in the presence of intervalley scattering, which is, however, suppressed due to the y-translation symmetry. This results in the observed transport suppression [26]. The very small but finite (10^{-8}) residual transmission across the MTB, as shown in the inset of fig. 6(a), can be considered as zero within the calculation accuracy.

We investigate the robustness of this phenomenon against short-range disorder, which is expected to induce intervalley scattering and activate transport. To this aim, we consider a large ribbon ($W = 50$ nm) with edge roughness and an MTB across its section. Figure 6(b) shows that the conductance is still suppressed at the top of the valence band, but there is a residual transmission due to intervalley scattering induced by the ribbon edges. Given the extremely small conductance, a residual contribution of edge state channels cannot be excluded. Note that, to be effective, intervalley scattering must occur at the grain boundary, when electrons pass from one grain to the other. Incidentally, at the top of the valence band and within the same grain, intervalley scattering is suppressed by the spin-valley locking mechanism. The conductance increases when including Anderson disorder along the MTB (over a width of

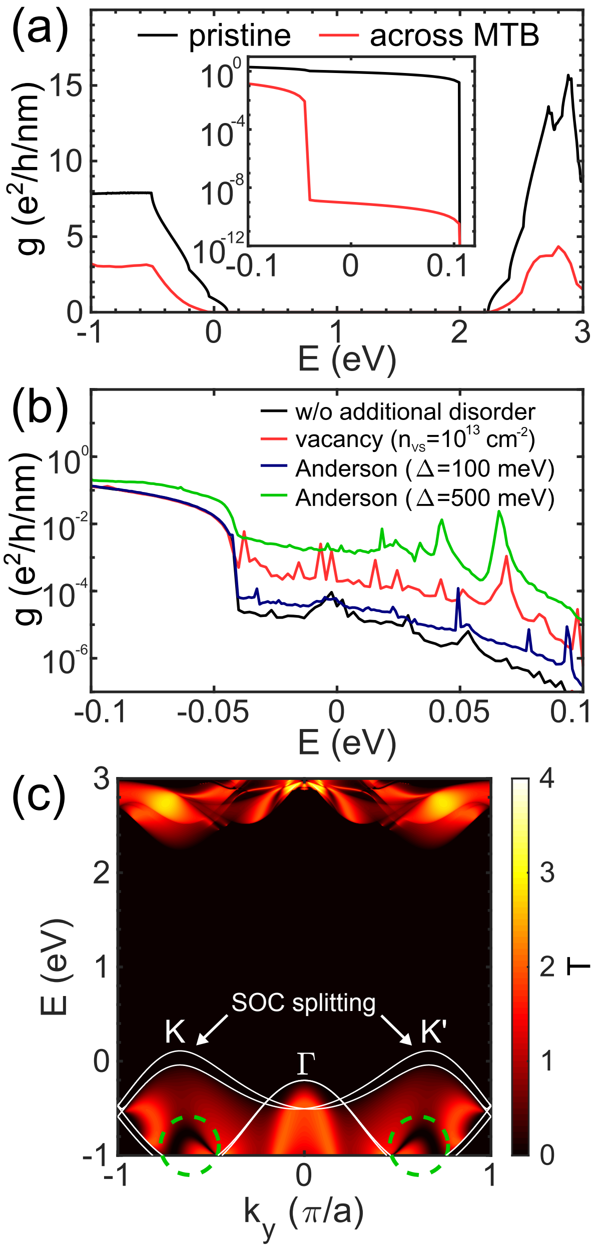

FIG. 6. (a) Main panel: Zero-temperature conductance *per* unit of width as a function of the electron energy for pristine 2D MoS_2 and in the presence of a transverse MTB. Inset: Conductance at the top of the valence band in logarithmic scale. (b) Zero-temperature conductance *per* unit of width at the top of the valence band for 50 nm-wide MoS_2 ribbons with a transverse MTB in the absence (black line) and in the presence of short-range disorders in the region of the MTB, namely sulfur vacancies over an 80-nm-long section and Anderson disorder over a 2-nm-wide stripe surrounding the MTB with different strengths. To suppress edge contribution to the transmission, we introduced edge roughness. (c) Transmission coefficient as a function of the wave number and the electron energy for 2D MoS_2 with a transverse MTB. The white lines correspond to the band profile of 2D MoS_2, while the dashed circles indicate the strong suppression of transmission in the valence band.

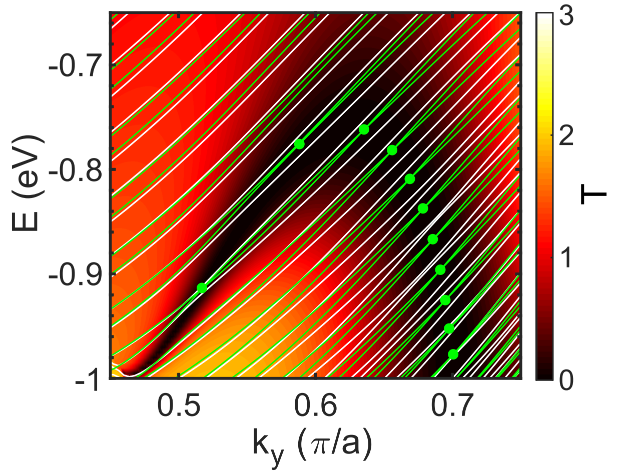

FIG. 7. Transmission coefficient as a function of the wave number and the electron energy in one of the two regions indicated by dashed circles in fig. 6(c). The band structure of for a 20 nm-wide zigzag ribbon with a periodic MTB without (green lines) and with (white lines) SOC is superimposed.

2 nm), see fig. 6(b), which strongly enhances intervalley scattering all along the grain boundary length. The conductance increase is larger for larger Anderson disorder strength Δ from 100 meV to 500 meV. A similar effect is observed in the presence of sulfur vacancies with density $n_{\mathrm{VS}} = 10^{13}$ cm^{-2}, whose extremely short-range nature entails a strong intervalley scattering. Note that our model does not consider the Hartree potential induced in the vicinity of MTB, whose estimation may be sensitive to the model details and which is expected to entail a further reduction of the transmission for energies close to the top of the valence band [21, 26]. This choice does not affect our physical analysis.

A further insight into the results of fig. 6(a) can be gained from the energy- and k_y-resolved transmission coefficient $T(E, k_y)$ reported in fig. 6(c). This figure clearly shows the different contributions of the K/K' valleys, close to the sides of the BZ, and of the Γ valley at the center. The result confirms the complete suppression of transport at energies between the two SOC-split topmost valence bands. Surprisingly enough, we observe a strong suppression of $T(E, k_y)$ at low energies in the valence band, as indicated by dashed circles. This behavior is related to the MTB effect of "cutting" the system into weakly coupled parts, as mentioned in Sec. II. At the energies and wave numbers where $T(E, k_y)$ is suppressed, the coupling between the two parts of the system on the sides of the MTB is very small. To support this interpretation, we superimpose the valence bands of a 20 nm-wide zigzag ribbon with a periodic MTB to the transmission coefficient. At first, we do not consider SOC, see the green lines in fig. 7. As discussed in Sec. II, the band structure is determined by the coupling of the subbands that reside on each side of the

MTB. Since the coupling is weak, we observe couples of split bands. Where the bands cross, see the green dots in the figure, the coupling between the two regions at the sides of the MTB is vanishing. This explains why the low transmission coefficient is exactly observed at these crossing points. Note that increasing the width of the ribbon would just increase the number of the subbands and crowd the crossing points along the lowest transmission region (not shown here), thus confirming the validity of this picture in the 2D limit. Introducing the SOC, see the white lines in fig. 7, makes the interpretation more convoluted due to the absence of the crossing points. This is because of the opposite spin-splitting energy on the states at two sides of the MTB for given K/K' valley, which again is a consequence of the spin-valley locking mechanism and the mirror symmetry.

In conclusion of this section, we would like to point out that transport properties of the polycrystalline MoS_2 can be highly dependent on the density of the grain boundaries, which may cause a severe degradation of the conductivity. Controlling the density of grain boundaries will be a significant factor for the use in electronic applications [18].

V. CONCLUSIONS

In summary, we have numerically investigated the transport properties of MoS_2 in the presence of an MTB. Along the grain boundary, conductive channels develop at energies within the band gap of 2D MoS_2. The conductance of these states is found to be sensitive to chalcogen vacancies, relatively robust against short-range Anderson disorder, and scarcely impacted by long-range disorder. On the other side, transport across the mirror grain boundary is significantly affected, and its analysis in terms of wave number dependent transmission reveals peculiar features of this grain boundary, as the separation of the ribbon into two weakly coupled narrower ribbons. Moreover, as already demonstrated in the literature [26], the transmission across the grain boundary is suppressed in the energy range of the spin-orbit splitting of the valence, due to spin-valley locking. However, we demonstrate that transmission is partially allowed as a consequence of the induced intervalley scattering in the presence of short-range disorder. Our results provide physical and quantitative insight into the interplay between grain boundaries and additional disorder. They could thus be beneficial to the design of electronic devices based on TMDs, in particular for the control of leakage current in field-effect transistors and the fabrication of 2D metallic contacts based on grain boundary networks.

ACKNOWLEDGMENTS

This work was supported in part by the French Agence Nationale de la Recherche via the LabEx Minos under Grant No. ANR-10-LABX-55-01.

Appendix A: *Ab initio* calculations

DFT calculations were carried out using the plane-wave basis set with a kinetic energy cutoff of 500 eV and the projector augmented-wave method, as implemented in the Vienna *Ab initio* Simulation Package [32, 33]. Generalized gradient approximation of the Perdew-Burke-Ernzerhof functional form [31] was used. The valence electron configurations were $4d$ and $5s$ for Mo, $3s$ and $3p$ for S, $1s$ for H. The BZs were sampled using Γ-centered k-point mesh. Monolayer MoS_2 was fully relaxed with a vacuum layer greater than 2 nm to avoid its interaction with periodic images along the x-axis. The resulting Mo-S bond length is 2.41 Å, while the y-axis lattice constant is 3.175 Å. A ribbon model with MTB was set up, whose width is 2.24 nm and the optimized lattice constant along the y-direction is 3.179 Å, very close to the pure monolayer case. At least 1 nm vacuum space was introduced in the x- and z-directions, and four hydrogen atoms *per* supercell were introduced to saturate the corresponding four S atoms on the edges. The electronic structures were calculated either with or without SOC.

For sulfur vacancy formation energy calculations, we enlarged the MTB supercell to 4 times along the y-axis. Therefore, one sulfur vacancy was introduced *per* 120-atom MoS_2 supercell. The missing sulfur atom was assumed to be in the solid α-S form, i.e., the sulfur chemical potential equals that in an $Fddd$ S_8 supercell.

Appendix B: Details and calibration of the tight-binding model

As mentioned in Sec. II, we made use of an 11-band Slater-Koster TB Hamiltonian with five d orbitals (d_{xy}, d_{yz}, d_{zx}, $d_{x^2-y^2}$, d_{z^2}) for the Mo atoms and three p orbitals (p_x, p_y, p_z) for the S atoms, which we indicate with S_b on the bottom layer and with S_t on the top layer. The TB Hamiltonian elements include on-site and hopping energies for S_t–S_b within the same unit cell, Mo–$S_{t,b}$ within each unit cell and its adjacent cells, and next-nearest-neighbor ones for Mo–Mo and S–S within adjacent cells. We adopted the Slater-Koster parameters reported in Ref. [35].

Even after the consideration of the strain effect on MTB as detailed in the main text, a further calibration of the TB model was required for tuning the energy of the MTB states. We illustrate here the calibration procedure. We analyzed the wave functions of the MTB states as resulting from the TB model, see fig. 8, and compared them with those obtained by DFT calculations. The shape of the MTB bands within the gap as well as the different spatial extension of the wave functions for states on bands ① and ② well match the DFT results [21, 30].

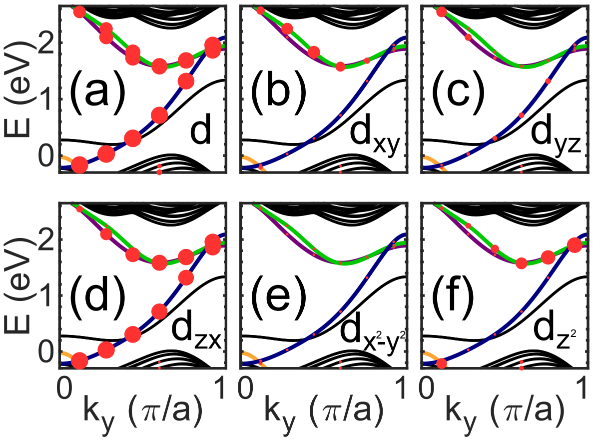

FIG. 8. Band structure obtained with the non-calibrated TB model and without SOC for the ribbon of fig. 1(b). MTB bands within the bulk gap are indicated in blue, green and purple lines. Orange lines display the MTB band above the bulk states at the Γ point. The MTB bands in blue and green lines correspond to bands ① and ② in fig. 1(b). Red circles denote the weight of molybdenum atoms in the MTB region. (a) Contribution of all d orbitals, (b) d_{xy}, (c) d_{yz}, (d) d_{zx}, (e) $d_{x^2-y^2}$, and (f) d_{z^2}. Contribution of S atoms to the MTB bands within the bulk gap is insignificant compared to that of Mo atoms and thus not displayed.

The bands corresponding to the edge states, whose details we are not interested in here, do not match those of the cited references, since they depend on the specific edge passivation. The main difference with DFT calculations is the energy downshift of band ①. By the analysis of the wave function composition, we observe that the main contributions to band ① come from orbitals d_{yz} and d_{zx}, see figs. 8(c) and 8(d), respectively. To shift the energy of band ①, we thus modified the on-site energies of the nearest Mo atoms on MTB by +1 eV for d_{zx} and +0.2 eV for d_{yz}. The extreme localization of band ① allows us to shift it without affecting the other bands. Note that an extra MTB band indicated by purple lines in fig. 8, which possesses the same orbital contribution as band ①, is also shifted upward to the bottom of and inside the conduction band. The other aspect to take into account is the presence of MTB states on the top of the valence band at the Γ point, which appears at even higher energies than the bulk states, see the orange lines in fig. 8. MTB states in the valence band in DFT, however, are located at lower energies at Γ [30]. Therefore we modified the on-site energies of the same Mo atoms by -0.3 eV for d_{xy} and -0.8 eV for d_{z^2} to shift down and calibrate the energy of the MTB states in the valence band.

Figure 9(a) shows the band structure of a MoS_2 ribbon with a periodic MTB along its axis obtained with the calibrated TB model. The MTB bands ① and ② within the bulk gap well reproduce those of the DFT calculation, see fig. 9(b). The MTB states outside the bulk gap, as well as the presence of MTB states below the edge of the valence band and close to the edge of the conduction band, also agree with the results of Ref. [30]. Furthermore, we observe spin degeneracy and anti-crossing between bands ① and ② for both the calibrated TB model and the DFT calculation.

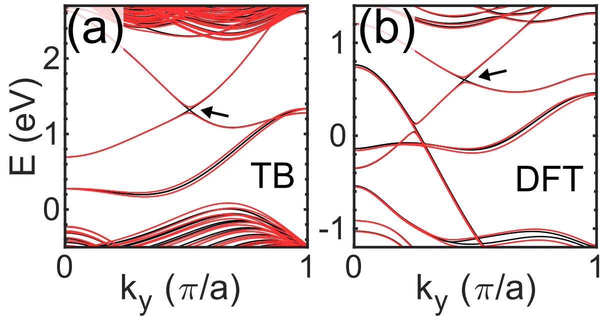

FIG. 9. (a) Band structure obtained with the calibrated TB model for the ribbon of fig. 1(b). The SOC-induced gap is indicated by an arrow. (b) Band structure obtained by DFT calculations for a ribbon with width $W = 2.2$ nm. The SOC-induced gap, indicated by an arrow, is ~60 meV, i.e., slightly narrower than in the TB case. A narrow ribbon width is considered to reduce the computational burden. The shape of the MTB bands is not significantly affected by the ribbon width, provided the ribbon is large enough to avoid the coupling between edge and MTB states. Black and red lines display the bands without and with SOC, respectively.

Appendix C: Details of the scaling analysis for Anderson disorder

To illustrate the scaling analysis performed to statistically analyze the transport regimes in the presence of Anderson disorder, we focus on the ribbon with width $W = 10$ nm and fix the disorder strength to $\Delta = 100$ meV. We select two representative energies, E=1 eV and E=1.8 eV for the scaling analysis of transport properties along MTB. As shown in fig. 4(b), $\langle T\rangle$ rapidly decreases when L increases for E=1 eV. This suggests the transport regime is localized, as confirmed by the linear decrease of the average logarithm of the transmission coefficient $\langle \ln T\rangle$ as a function of L, see fig. 10(a). The localization length is then extracted according to eq. (5), which gives $\xi = 58$ nm for the selected energy. Also, fig. 10(b) shows the typical [46] Gaussian frequency distribution of $\ln T$ with $|\Delta \ln T \ / \ \langle \ln T\rangle| < 1$, where $\Delta \ln T$ is the standard deviation. For E=1.8 eV, $\langle T\rangle$ decreases more slowly for increasing L, thus suggesting a diffusive transport regime. This is confirmed by fig. 10(c), which shows the inverse of the average transmission coefficient $\langle T\rangle$ as a function of the length L. Its linear scaling allows us to extract the mean free path according to eq. (6), $\ell = 750$ nm for the given energy. Moreover, we observe a typical [46] Gaussian distribution with $\Delta T/\langle T\rangle < 1$,

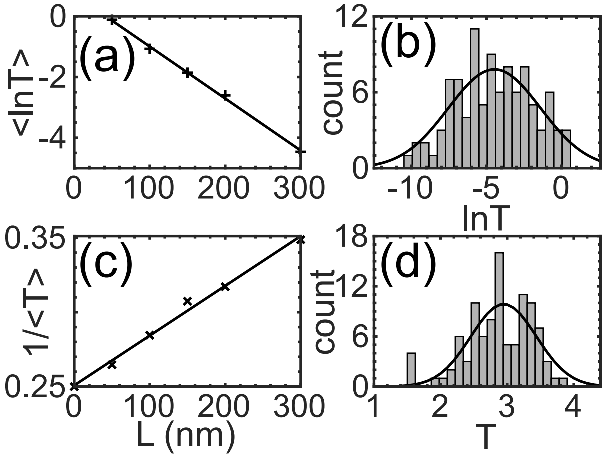

FIG. 10. Scaling analysis of the localized (a), (b) and diffusive (c), (d) transport regimes, for Anderson disorder with $\Delta = 100$ meV. (a) Average logarithm of the transmission coefficient as a function of L at $E = 1$ eV, which corresponds to the energy region A in fig. 4(b). The continuous line shows the linear fit. The estimated localization length is $\xi \approx 58$ nm. (b) Frequency distribution of ln$T$ for $L = 300$ nm at the same energy. (c) Inverse of the average the transmission coefficient as a function of L at $E = 1.8$ eV chosen within the energy region C in fig. 4 (b). The continuous line shows the linear fit. The estimated mean free path is $\ell \approx 750$ nm. (d) Frequency distribution of T for $L = 300$ nm at the same energy.

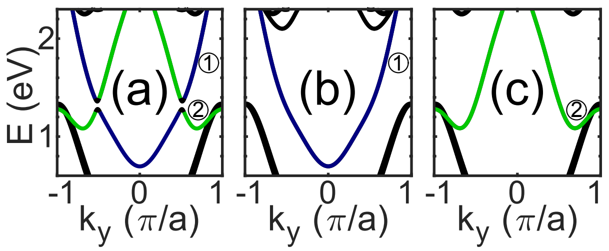

FIG. 11. Separation of the MTB bands, ① (green lines) and ② (blue lines) by modification of the Hamiltonian. (a) Band structure without any modification for the ribbon of fig. 1(b). (b), (c) Band structures obtained by modification of the Hamiltonian for isolating bands ① and ②, respectively.

where ΔT is the standard deviation of T, see fig. 10(d).

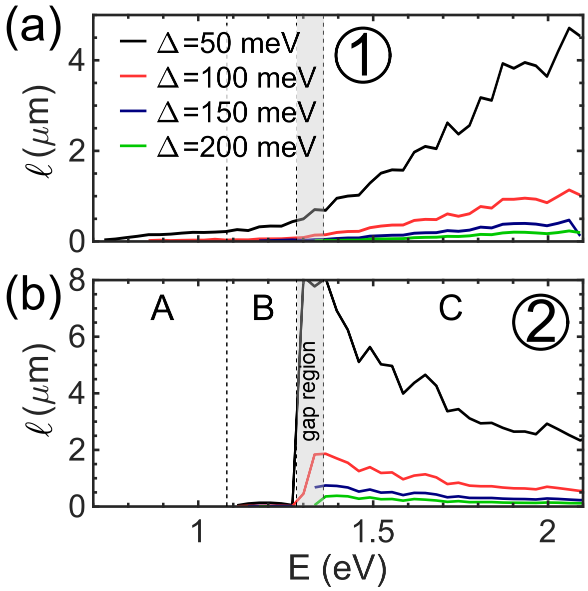

FIG. 12. Mean free path as a function of the electron energy in the presence of Anderson disorder with strength Δ varying from 50 meV to 200 meV. The individual mean free paths of (a) band ① and (b) band ②, calculated starting from the modified Hamiltonian corresponding to the band structures in figs. 11(b) and 11(c), respectively.

Appendix D: Details of the analysis in terms of individual MTB bands in the case of Anderson disorder

As discussed in Sec. II, the total transmission along MTB is related to the independent contribution of the two MTB bands within the bulk gap, bands ① and ②. Even though the SOC entails a weak coupling between them and thus induces a small gap, their contributions in terms of d orbitals of the nearest Mo atoms on MTB is preserved, except for energies close to the SOC-induced gap, where the two bands hybridize. To better understand the contribution of each band to transport properties, we artificially separate bands ① and ② by modifying the Hamiltonian to shift alternatively one of the two bands at higher energy and isolate the contribution of the other. To this aim, we only modify the on-site energies of the specific d orbitals of the Mo atoms close to the MTB contributing to the states of the chosen band. To isolate the contribution to transport of band ①, band ② is shifted upward by increasing the on-site energies of the d_{xy} and the d_{z^2} orbitals by 0.5 eV and 2.0 eV, respectively. To isolate the contribution to transport of band ②, band ① is shifted upward by increasing the on-site energy of the d_{zx} orbital by 3.0 eV. The resulting modified band structures are reported in fig. 11. Compared to the unmodified band structure shown in fig. 11(a), only one band remains in its initial position, while the other one enters into the conduction band, thus not contributing to transport in the energy range of the bulk band gap, see figs. 11(b) and fig. 11(c).

As discussed in Sec. III B, except for the region close to the SOC gap, the average transmission coefficient $\langle T \rangle$ turns out to be close to the sum of the two contributions $\langle T_1 \rangle + \langle T_2 \rangle$, see fig. 4(d). Figure 12 reports the mean free path of each band as a function of the energy E. At lower energies corresponding to regions A and B in fig. 4(b), band ① exhibits a relatively large mean free path compared to ②. This behavior indicates the main contribution of band ① to transport. For higher energies above the SOC-induced gap, on the other hand, both bands are activated and contribute to the diffusive transport regime with relatively large mean free paths. The mean free path corresponding to band ① is shorter than for band ②, and it becomes longer for $E > 1.8$ eV.

[1] K. S. Novoselov, Electric Field Effect in Atomically Thin Carbon Films, Science **306**, 666 (2004).

[2] P. Miró, M. Audiffred, and T. Heine, An atlas of two-dimensional materials, Chemical Society Reviews **43**, 6537 (2014).

[3] G. Fiori, F. Bonaccorso, G. Iannaccone, T. Palacios, D. Neumaier, A. Seabaugh, S. K. Banerjee, and L. Colombo, Electronics based on two-dimensional materials, Nature Nanotechnology **9**, 768 (2014).

[4] F. Schwierz, J. Pezoldt, and R. Granzner, Two-dimensional materials and their prospects in transistor electronics, Nanoscale **7**, 8261 (2015).

[5] F. Schwierz, Graphene transistors, Nature Nanotechnology **5**, 487 (2010).

[6] F. Giannazzo, G. Greco, F. Roccaforte, and S. Sonde, Vertical Transistors Based on 2D Materials: Status and Prospects, Crystals **8**, 70 (2018).

[7] D. Logoteta, M. G. Pala, J. Choukroun, P. Dollfus, and G. Iannaccone, A Steep-Slope MoS_2-Nanoribbon MOSFET Based on an Intrinsic Cold-Contact Effect, IEEE Electron Device Letters **40**, 1550 (2019).

[8] H. Simchi, M. Simchi, M. Fardmanesh, and F. M. Peeters, Phase transition and field effect topological quantum transistor made of monolayer MoS_2, Journal of Physics: Condensed Matter **30**, 235303 (2018).

[9] X. Cui, G.-H. Lee, Y. D. Kim, G. Arefe, P. Y. Huang, C.-H. Lee, D. A. Chenet, X. Zhang, L. Wang, F. Ye, F. Pizzocchero, B. S. Jessen, K. Watanabe, T. Taniguchi, D. A. Muller, T. Low, P. Kim, and J. Hone, Multi-terminal transport measurements of MoS_2 using a van der Waals heterostructure device platform, Nature Nanotechnology **10**, 534 (2015).

[10] Q. H. Wang, K. Kalantar-Zadeh, A. Kis, J. N. Coleman, and M. S. Strano, Electronics and optoelectronics of two-dimensional transition metal dichalcogenides, Nature Nanotechnology **7**, 699 (2012).

[11] B. Radisavljevic, A. Radenovic, J. Brivio, V. Giacometti, and A. Kis, Single-layer MoS_2 transistors, Nature Nanotechnology **6**, 147 (2011).

[12] L. Yu, Y.-H. Lee, X. Ling, E. J. G. Santos, Y. C. Shin, Y. Lin, M. Dubey, E. Kaxiras, J. Kong, H. Wang, and T. Palacios, Graphene/MoS_2 Hybrid Technology for Large-Scale Two-Dimensional Electronics, Nano Letters **14**, 3055 (2014).

[13] S. Wachter, D. K. Polyushkin, O. Bethge, and T. Mueller, A microprocessor based on a two-dimensional semiconductor, Nature Communications **8**, 14948 (2017).

[14] A. M. van der Zande, P. Y. Huang, D. A. Chenet, T. C. Berkelbach, Y. You, G.-H. Lee, T. F. Heinz, D. R. Reichman, D. A. Muller, and J. C. Hone, Grains and grain boundaries in highly crystalline monolayer molybdenum disulphide, Nature Materials **12**, 554 (2013).

[15] S. Najmaei, Z. Liu, W. Zhou, X. Zou, G. Shi, S. Lei, B. I. Yakobson, J.-C. Idrobo, P. M. Ajayan, and J. Lou, Vapour phase growth and grain boundary structure of molybdenum disulphide atomic layers, Nature Materials **12**, 754 (2013).

[16] W. Zhou, X. Zou, S. Najmaei, Z. Liu, Y. Shi, J. Kong, J. Lou, P. M. Ajayan, B. I. Yakobson, and J.-C. Idrobo, Intrinsic Structural Defects in Monolayer Molybdenum Disulfide, Nano Letters **13**, 2615 (2013).

[17] K. Hsieh, V. Kochat, X. Zhang, Y. Gong, C. S. Tiwary, P. M. Ajayan, and A. Ghosh, Effect of Carrier Localization on Electrical Transport and Noise at Individual Grain Boundaries in Monolayer MoS_2, Nano Letters **17**, 5452 (2017).

[18] S. Najmaei, M. Amani, M. L. Chin, Z. Liu, A. G. Birdwell, T. P. O'Regan, P. M. Ajayan, M. Dubey, and J. Lou, Electrical Transport Properties of Polycrystalline Monolayer Molybdenum Disulfide, ACS Nano **8**, 7930 (2014).

[19] T. H. Ly, D. J. Perello, J. Zhao, Q. Deng, H. Kim, G. H. Han, S. H. Chae, H. Y. Jeong, and Y. H. Lee, Misorientation-angle-dependent electrical transport across molybdenum disulfide grain boundaries, Nature Communications **7**, 10426 (2016).

[20] H. Liu, L. Jiao, F. Yang, Y. Cai, X. Wu, W. Ho, C. Gao, J. Jia, N. Wang, H. Fan, W. Yao, and M. Xie, Dense network of one-dimensional midgap metallic modes in monolayer $MoSe_2$ and their spatial undulations, Physical Review Letters **113**, 066105 (2014).

[21] O. Lehtinen, H.-P. Komsa, A. Pulkin, M. B. Whitwick, M.-W. Chen, T. Lehnert, M. J. Mohn, O. V. Yazyev, A. Kis, U. Kaiser, and A. V. Krasheninnikov, Atomic Scale Microstructure and Properties of Se-Deficient Two-Dimensional $MoSe_2$, ACS Nano **9**, 3274 (2015).

[22] X. Zou, Y. Liu, and B. I. Yakobson, Predicting Dislocations and Grain Boundaries in Two-Dimensional Metal-Disulfides from the First Principles, Nano Letters **13**, 253 (2013).

[23] Y. Ma, S. Kolekar, H. C. Diaz, J. Aprojanz, I. Miccoli, C. Tegenkamp, and M. Batzill, Metallic Twin Grain Boundaries Embedded in $MoSe_2$ Monolayers Grown by Molecular Beam Epitaxy, ACS Nano **11**, 5130 (2017).

[24] H. C. Diaz, Y. Ma, R. Chaghi, and M. Batzill, High density of (pseudo) periodic twin-grain boundaries in molecular beam epitaxy-grown van der Waals heterostructure: $MoTe_2/MoS_2$, Applied Physics Letters **108**, 191606 (2016).

[25] M. Ghorbani-Asl, A. N. Enyashin, A. Kuc, G. Seifert, and T. Heine, Defect-induced conductivity anisotropy in MoS_2 monolayers, Physical Review B **88**, 1 (2013).

[26] A. Pulkin and O. V. Yazyev, Spin- and valley-polarized transport across line defects in monolayer MoS_2, Physical Review B **93**, 041419(R) (2016).

[27] M. Büttiker, Y. Imry, R. Landauer, and S. Pinhas, Generalized many-channel conductance formula with application to small rings, Physical Review B **31**, 6207 (1985).

[28] S. Barja, S. Wickenburg, Z.-F. Liu, Y. Zhang, H. Ryu, M. M. Ugeda, Z. Hussain, Z.-X. Shen, S.-K. Mo, E. Wong, M. B. Salmeron, F. Wang, M. F. Crommie, D. F. Ogletree, J. B. Neaton, and A. Weber-Bargioni, Charge density wave order in 1D mirror twin boundaries

of single-layer $MoSe_2$, Nature Physics **12**, 751 (2016).

[29] Y. Ma, H. C. Diaz, J. Avila, C. Chen, V. Kalappattil, R. Das, M.-H. Phan, T. Čadež, J. M. P. Carmelo, M. C. Asensio, and M. Batzill, Angle resolved photoemission spectroscopy reveals spin charge separation in metallic $MoSe_2$ grain boundary, Nature Communications **8**, 14231 (2017).

[30] W. Jolie, C. Murray, P. S. Weiß, J. Hall, F. Portner, N. Atodiresei, A. V. Krasheninnikov, C. Busse, H.-P. Komsa, A. Rosch, and T. Michely, Tomonaga-Luttinger Liquid in a Box: Electrons Confined within MoS_2 Mirror-Twin Boundaries, Physical Review X **9**, 011055 (2019).

[31] J. P. Perdew, K. Burke, and M. Ernzerhof, Generalized Gradient Approximation Made Simple, Physical Review Letters **77**, 3865 (1996).

[32] G. Kresse and J. Furthmüller, Efficiency of ab-initio total energy calculations for metals and semiconductors using a plane-wave basis set, Computational Materials Science **6**, 15 (1996).

[33] G. Kresse and J. Furthmüller, Efficient iterative schemes forab initiototal-energy calculations using a plane-wave basis set, Physical Review B **54**, 11169 (1996).

[34] J. C. Slater and G. F. Koster, Simplified LCAO method for the periodic potential problem, Physical Review **94**, 1498 (1954).

[35] E. Ridolfi, D. Le, T. S. Rahman, E. R. Mucciolo, and C. H. Lewenkopf, A Tight-Binding Model For MoS_2 Monolayers, Journal of Physics: Condensed Matter **27**, 365501 (2015).

[36] A. C. Dias, F. Qu, D. L. Azevedo, and J. Fu, Band structure of monolayer transition-metal dichalcogenides and topological properties of their nanoribbons: Next-nearest-neighbor hopping, Physical Review B **98**, 075202 (2018).

[37] R. Roldán, M. P. López-Sancho, F. Guinea, E. Cappelluti, J. A. Silva-Guillén, and P. Ordejón, Momentum dependence of spin-orbit interaction effects in single-layer and multi-layer transition metal dichalcogenides, 2D Materials **1**, 034003 (2014).

[38] H. Rostami, R. Roldán, E. Cappelluti, R. Asgari, and F. Guinea, Theory of Strain in Single-Layer Transition Metal Dichalcogenides, Physical Review B **92**, 195402 (2015).

[39] S.-F. Chen and Y.-R. Wu, Electronic properties of MoS_2 nanoribbon with strain using tight-binding method, physica status solidi (b) **254**, 1600565 (2017).

[40] Y. Meir and N. S. Wingreen, Landauer formula for the current through an interacting electron region, Phys. Rev. Lett. **68**, 2512 (1992).

[41] A. Cresti, R. Farchioni, G. Grosso, and G. Pastori Parravicini, Keldysh-Green function formalism for current profiles in mesoscopic systems, Physical Review B **68**, 075306 (2003).

[42] F. Triozon and P. Dollfus, *Simulation of Transport in Nanodevices* (ISTE and John Wiley & Sons, 2016).

[43] J. Park, M. Mouis, F. Triozon, and A. Cresti, Impact of edge roughness on the electron transport properties of MoS_2 ribbons, Journal of Applied Physics **124**, 224302 (2018).

[44] H. Qiu, T. Xu, Z. Wang, W. Ren, H. Nan, Z. Ni, Q. Chen, S. Yuan, F. Miao, F. Song, G. Long, Y. Shi, L. Sun, J. Wang, and X. Wang, Hopping transport through defect-induced localized states in molybdenum disulphide, Nature Communications **4**, 2642 (2013).

[45] P. W. Anderson, Absence of diffusion in certain random lattices, Physical Review **109**, 1492 (1958).

[46] R. Avriller, S. Roche, F. Triozon, X. Blase, and S. Latil, Low-dimensional quantum transport properties of chemically-disordered carbon nanotubes: From weak to strong localization regimes, Modern Physics Letters B **21**, 1955 (2007).

[47] S. Adam, S. Jung, N. N. Klimov, N. B. Zhitenev, J. A. Stroscio, and M. D. Stiles, Mechanism for puddle formation in graphene, Physical Review B **84**, 235421 (2011).

[48] D. V. Tuan, F. Ortmann, A. W. Cummings, D. Soriano, and S. Roche, Spin dynamics and relaxation in graphene dictated by electron-hole puddles, Scientific Reports **6**, 21046 (2016).